

Article

Source and Enrichment of Toxic Elements in Coal Seams around Mafic Intrusions: Constraints from Pyrites in the Yuandian Coal Mine in Anhui, Eastern China

Yanfei An ^{1,*}, Lingling Liu ¹, Mina Wang ¹, Shuo Zheng ^{1,*}, Yuanjie Guo ¹, Shuai Zhang ¹ and Chunkit Lai ^{2,3} 

¹ School of Resource and Environment Engineering, Anhui University, Hefei 230601, China; tkyglll@163.com (L.L.); wmn522@163.com (M.W.); guoyuanjie852@163.com (Y.G.); zsl996sysu@163.com (S.Z.)

² Faculty of Science, University of Brunei Darussalam, Gadong BE1410, Brunei Darussalam; chunkitl@utas.edu.au

³ Centre for Excellence in Ore Deposits (CODES), University of Tasmania, Hobart 7001, Australia

* Correspondence: any@ahu.edu.cn (Y.A.); xyzheng0407@163.com (S.Z.); Tel.: +86-13956067105 (Y.A.)

Received: 7 March 2018; Accepted: 8 April 2018; Published: 17 April 2018



Abstract: Pyrite, a mineral that can cause potential environmental issues in coal mining, is commonly found in coal seams around intrusions. In this paper, pyrites from the Yuandian Coal Mine (Huaibei Coalfield, Anhui, Eastern China) were studied using SEM, Raman and LA-ICP-MS. The pyrite morphologic and geochemical data suggest that (1) four pyrite generations are present (framboidal sedimentary pyrites (Py I) in the original coal, coarse-grained magmatic pyrites (Py II) in the intruding diabase, fine-grained metamorphic pyrites (Py III) in the intrusive contact aureole, and spheroid/vein hydrothermal pyrites (Py IV) in the cokeite); and (2) concentrations of cobalt, nickel, arsenic, selenium, lead and copper in the metamorphic pyrites are much higher than the other pyrite generations. We propose that mafic magmatism is the main contributor of the toxic elements to the intrusion-related cokeite at Yuandian.

Keywords: Yuandian Coal Mine; pyrite generations; morphology; toxic elements; Eastern China

1. Introduction

The thermal metamorphism in coal seams around intrusions has received increasing attention in recent years [1–16], with studies dedicated mainly to intrusion-related cokeite [17–19], gas outbursts [20–22], geochemical components (especially toxic metals) and anomalies [23–35]. It has been found that thermal metamorphism not only separates coal into gas and cokeite [17–22], but also alters the chemical compositions of coal seams via magmatic-derived components [23–34]. Although some studies have linked thermal metamorphism with the strong enrichment of toxic elements in coal seams [28–38], the elemental source and enrichment mechanism remains controversial [36–38]. Some authors have argued that most of the toxic elements are magma-derived [28–34] and that their enrichments are closely related to the formation of secondary sulphides (such as pyrite, chalcopyrite, galena and sphalerite) [29–37]. Meanwhile, some authors suggested that metamorphism/metasomatism could not affect immobile elements such as rare earth elements (REEs) [27–30,38]. In this paper, we tackle this issue from a pyrite mineralogical and geochemical perspective. Pyrite occurs in different rock types in the mine (coal seams, magmatic intrusions and the contact metamorphic aureole between them), allowing systematic mineral geochemical comparison

between these different lithologies [39–45]. In addition, many toxic elements (notably, As, Sb and Pb) are hosted in pyrite [32–47]. Using SEM, Raman and LA-ICP-MS analyses, we first identified four pyrite generations from the Yuandian Mine (Huaibei Coalfield, Anhui, China), each with a very different morphology and chemistry. We proposed that the toxic elements at the Yuandian Mine were mainly derived from the mafic intrusions.

2. Geological Setting, Samples and Methods

2.1. Geological Setting

The Yuandian Coal Mine is located in the Northern Anhui Province, Eastern China (Figure 1a). The coal-bearing formations are located in the intersection of the Subei fault and the Fengxian–Guoyang fault (Figure 1b), hosted in upper Palaeozoic clastic and carbonate sequences [14]. Eleven layers of coal seams are distributed in the Carboniferous Taiyuan and Shanxi groups and the Permian Shihezi group [9]. Many diabasic–gabbroic sills have been documented in these coal seams [20]. For seams in the middle part of the stratigraphy, for example, coal seam VIII, intrusion-related cokeite is found interlayered with the diabasic–gabbroic sills. Within coal seam VIII, there are residual (unaffected) coal seams (2.97 m thick) in the lower part of the seam (Figure 1c). The maximum vitrinite reflectance is about 1.53–2.06%, the ash content is about 8.2–14.7%, the volatile matter is about 7.83–8.37%, the moisture content is about 0.59–0.72%, and the carbon content is about 77.7–83.1%. For the intrusion-related cokeite (>0.95 m thick) in the upper part of the seam, the ash content is about 19.5–24.9%, the volatile matter is about 6.58–7.39%, the moisture content is about 0.54–0.66%, and the carbon content is about 64.7–76.5%.

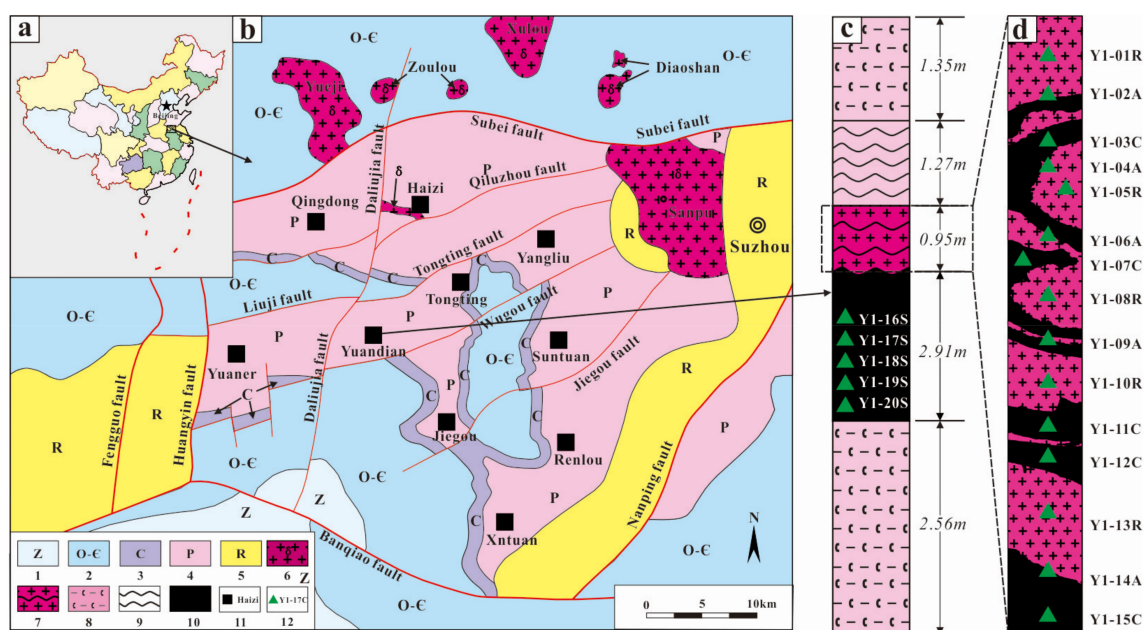


Figure 1. Location of the Yuandian Coal Mine in the Huaibei Coalfield, Anhui, China. Map of China, showing the location of the Huaibei Coalfield (a), regional geological map of the Yuandian Coal Mine (b), stratigraphy of coal seam VIII (c) and sampling locations (green triangle) (d). (1) Sinian, (2) Cambrian–Ordovician, (3) Devonian, (4) Permian, (5) Tertiary, (6) diabase, (7) intrusion-related cokeite, (8) shale, (9) schist, (10) coal seam, (11) coal mine, (12) sampling location and number.

2.2. Pyrite Sampling

A total of twenty core samples (diabase, coal, metamorphic aureole, cokeite and unaffected coal) were collected from drill hole no. 2016-6 in the Yuandian Coal Mine, Huaibei coal fields. Among these samples, Y1-01R, Y1-05R, Y1-08R, Y1-10R and Y1-13R were collected from diabase;

Y1-02A, Y1-04A, Y1-06A, Y1-09A and Y1-14A were from metamorphic aureole; Y1-03C, Y1-07C, Y1-11C, Y1-12C and Y1-15C were from cokeite; and Y1-16S, Y1-17S, Y1-18S, Y1-19S and Y1-20S were collected from the unaffected coal from -2 m away from the diabase mass. The sampling locations are shown in Figure 1c,d. The samples were prepared in polished slabs/thin sections for petrographic observations (50 points) under plane/cross polarized and reflected light under the microscope.

2.3. Occurrence of Pyrite

In the coal mine, intrusion-related layered cokeite from coal seam VIII is in contact with micro diabasic sills along a narrow metamorphic aureole (Figure 2a). The diabase comprises plagioclase ($>85\%$) and pyroxene ($<15\%$) (Figure 2b), with the grain sizes changing progressively from medium-fine to very fine near the chilled margin (Figure 2c). The cokeite is composed of porous coke, mosaic carbon and microspheric carbon with high reflectance and anisotropy (Figure 2d). Pyrites in the diabase, cokeite and metamorphic aureole appear very differently—pyrites in the diabase occur as large subhedral grains (>200 μm in size) or thin rims around plagioclase (Figure 2e); pyrites in the metamorphic aureole are mainly fine-grained (<30 μm) and scattered around plagioclase (Figure 2f). Pyrites in the cokeite occur either as bands (>500 μm long and several microns wide) or spherical aggregates (20–100 μm) (Figure 2g).

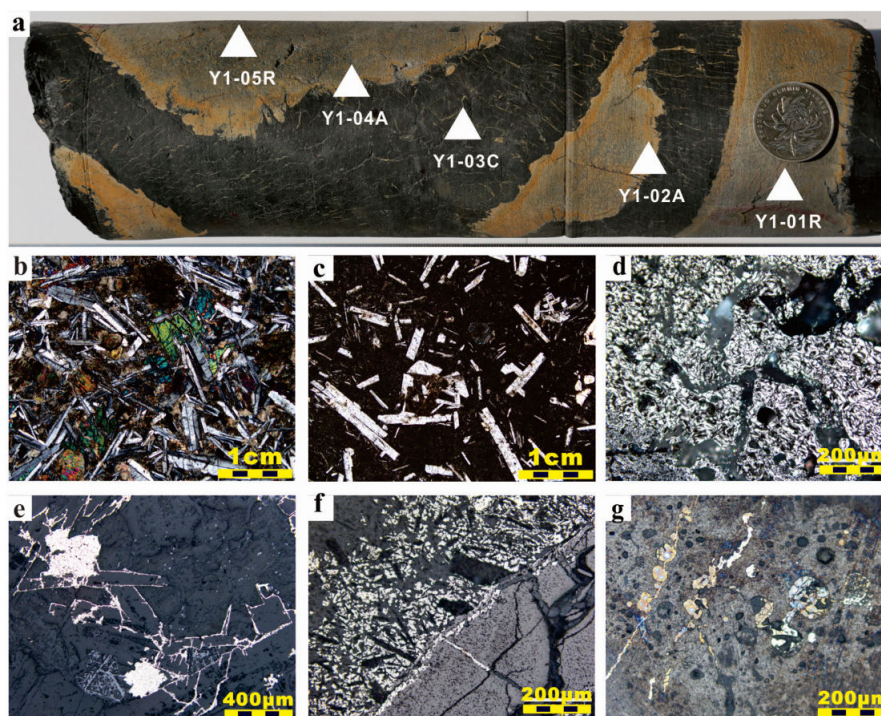


Figure 2. Photographs and photomicrographs of intrusion-related cokeite and pyrite from the Yuandian Coal Mine. (a) Hand-specimen of magma cokeite in seam VIII; (b) photomicrograph of a diabasic sill (Y1-01R) (+); (c) photomicrograph of a diabasic sill (Y1-02A) (−); (d) photomicrograph of cokeite (Y1-03C) (reflected light); (e) photomicrograph of coarse-grained pyrites in diabase (Y1-05R) (reflected light); (f) photomicrograph of fine-grained pyrites in metamorphic aureole (Y1-04A) (reflected light); (g) photomicrograph of spherical pyrites in cokeite (Y1-03C) (reflected light).

2.4. Analytical Procedures of Pyrite

Pyrite samples were collected from boreholes in the Yuandian Coal Mine, and thin sections were prepared for the Raman spectroscopic analysis at the Instrument Analysis and Research Center of Anhui University. The samples were also observed using SEM (scanning electron microscopy) and their chemistry was determined using LA-ICP-MS (laser ablation inductively coupled plasma mass

spectrometry) at the Laboratory of Sample Solution in Wuhan. A scanning electron microscope (JSM-IT100, JEOL Ltd., Tokyo, Japan), coupled with an energy-dispersive X-ray spectrometer (X-MAX020, Oxford Instruments, Oxford, UK), was used to study the mineral morphology and elemental distribution. The samples were carbon-coated using a Quorum Q150T ES sputtering coater. The working distance of the SEM-EDS was 10 mm, the beam voltage was 20.0 kV, the aperture was 6 nm and the spot size was 5 nm. The images were captured via a retractable solid state backscattered electron detector. Laser Confocal Raman Microspectrometry (LC-Raman, InVia-Reflex, Renishaw Co., Wotton-under-Edge, UK) was used to determine the spectral characteristics of pyrites, excited by the 532 nm line of an argon ion laser with 25 mW power and using a 50 μm slit of the Renishaw InVia Micro-Raman instrument. The intrinsic resolution of the spectrometer was 1.0 cm^{-1} and calibrations were accurate to 0.15 cm^{-1} , with the scanning range being $100\text{--}500\text{ cm}^{-1}$. The LA-ICP-MS system comprised an Agilent 7700 ICP-MS (Agilent Technologies, Santa Clara, CA, USA) coupled with a Resonetic RESOLUTION M-50 ArF-Excimer laser source ($\lambda = 193\text{ nm}$) (Coherent Inc., Santa Clara, CA, USA). The laser energy was 80 mJ with a frequency of 10 Hz and an ablation spot size of 44 μm . Both a double-volume sampling cell and a Squid pulse smoothing device were used to improve the data quality. The ablated aerosol was carried to the ICP source with He gas. Trace elements contents were calculated using the software ICPMS DataCal (version 10.2) (developed by the China University of Geosciences). The detection limits of most trace elements were 2–8 ppb, except for some elements, including Cr, Ni, Cu and Zn (detection limit: 1–5 ppm). The accuracy of the analysis was mostly better than 5%.

3. Results

3.1. SEM

SEM back scattered electron (BSE) imaging of the pyrites from the studied samples appeared very differently. Pyrite crystals and pyrite veinlets in the diabase can be divided the coarse-grained and veinlet types (Figure 3a). The former is euhedral-subhedral ($>200\text{ }\mu\text{m}$), whilst the latter occurs as fine veins ($<20\text{ }\mu\text{m}$ wide) around plagioclase (Figure 3b). While the boundaries between the coarse-grained pyrites and plagioclase are straight, those between the vein pyrites and plagioclase are irregular (Figure 3c). Pyrite crystals and pyrite veinlets in the metamorphic aureole can be divided into the fine-grained and veinlet types (Figure 3d). Fine-grained pyrites were mainly distributed in the groundmass of the diabase chilled margin, but not in either cokeite or phenocrysts in the chilled margin (Figure 3e). Only a few vein-type pyrites were found in the rim of mesocarbon microbeads in cokeite. Pyrite crystals and pyrite veinlets in cokeite occurred mainly as veinlets or spherical aggregates (Figure 3f). Pyrite veins commonly converged into bands of 500 μm long and several μm wide (Figure 3g). Spherical pyrite aggregates mainly filled in the pores of cokeite and encapsulated a large number of mesocarbon microbeads (MCMB) (Figure 3h). Pyrites in unaffected coal distal from the diabasic intrusion occurred dominantly as framboidal aggregates with a diameter of about 10 μm (Figure 3i). There were no fissures, and pore filled pyrites were found in the unaffected coal.

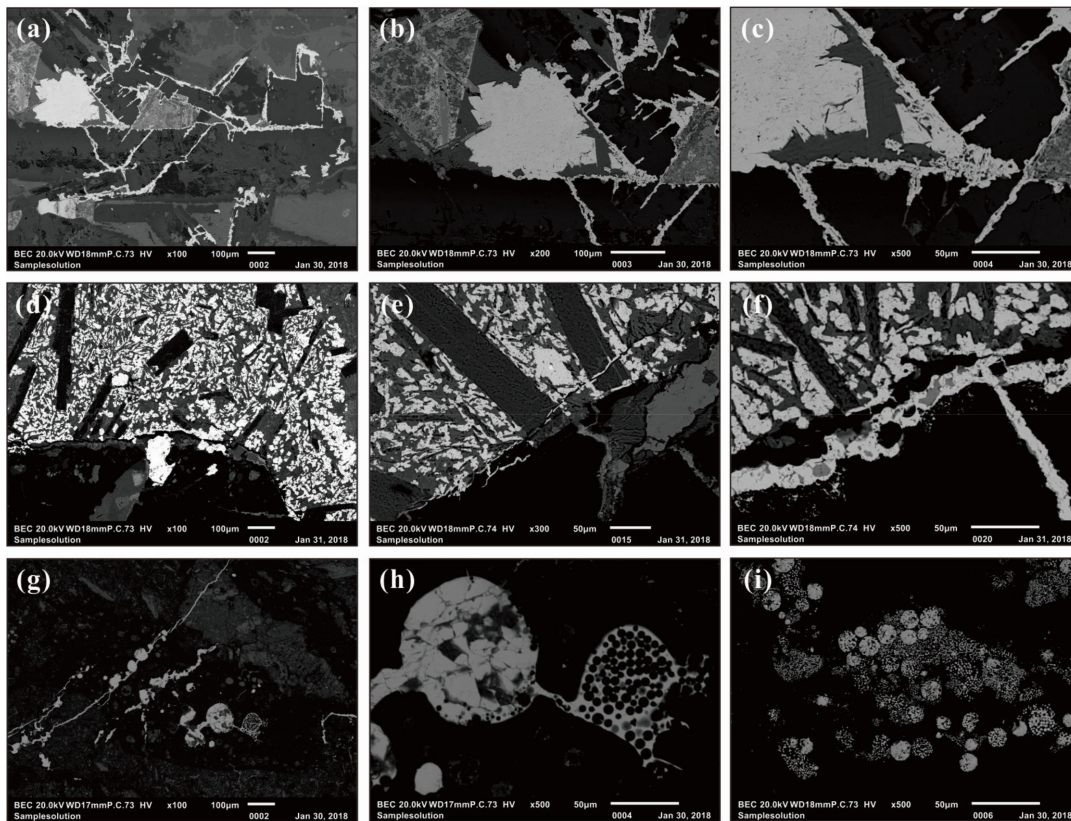


Figure 3. Back scattered electron image of pyrites from the Yuandian Coal Mine: (a) coarse-grained subhedral pyrites and thin pyrite veinlets around plagioclase in diabase (Y1-05R, 100×); (b) pyrite veinlets in the fractures of plagioclase (Y1-05R, 200×); (c) straight edge of coarse-grained pyrites (Y1-05R, 500×); (d) fine-grained pyrites around feldspar in metamorphic aureole (Y1-04A, 100×); (e) densely-disseminated pyrites in the groundmass at the diabase chilled margin (Y1-04A, 200×); (f) pyrites encircle and crosscut mesocarbon microbeads in metamorphic aureole (Y1-04A, 500×); (g) fine pyrite veinlets and spherical pyrite aggregates in cokeite (Y1-03C, 100×); (h) pyrites fill in pores and encapsulate mesocarbon microbeads in cokeite (Y1-03C, 500×); (i) disseminated pyrites and framboidal pyrites in unaffected coal (Y1-18S, 500×).

3.2. Raman

The Raman spectra of pyrites from the diabasic intrusion, metamorphic aureole, cokeite and unaffected coal are shown in Figure 4. The figure shows that three distinct Raman active modes, matching the previously published activity of $\text{Fe}[\text{S}_2]^{2-}$ Libérational Motion (Eg), $\text{Fe}[\text{S}_2]^{2-}$ Stretching Motion (Ag) and S–S Stretching Motion (Tg), are observed in all diagrams. However, there were clear differences in terms of the spectral intensity, frequency and shape. In order to facilitate identification, all Eg modes and Ag modes were incorporated into a correlation diagram (Figure 4) and transformed into Raman shift ($\Delta\nu$), mode intensity (I) and half width at half maximum (FWHM) data by Lorenz fitting (Table 1).

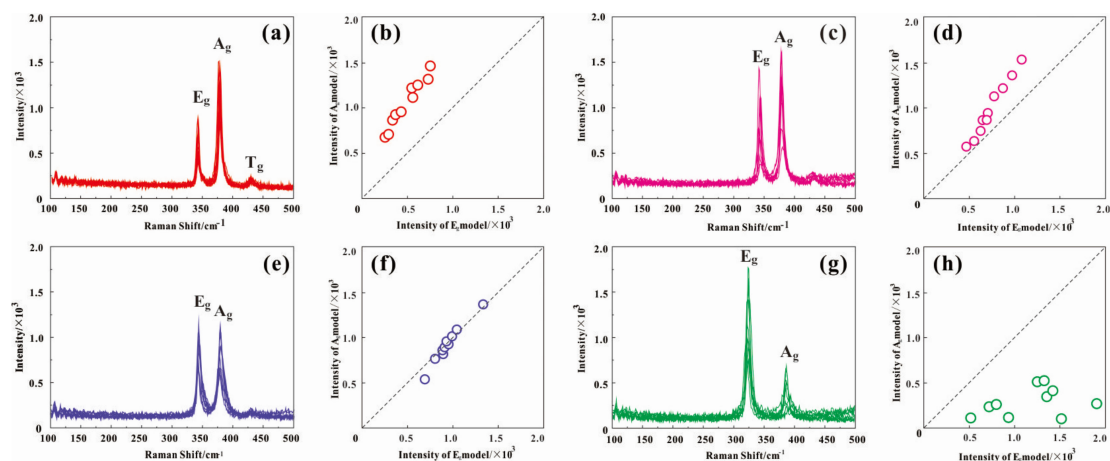


Figure 4. Raman spectra and correlogram of the Eg model and Ag model of the pyrites in (a,b) diabase (Y1-01R-1, Y1-01R-2, Y1-05R-1, Y1-05R-2, Y1-08R-1, Y1-08R-2, Y1-10R-1, Y1-08R-2, Y1-13R-1, Y1-13R-2); (c,d) metamorphic aureole (Y1-02A-1, Y1-02A-2, Y1-04A-1, Y1-04A-2, Y1-06A-1, Y1-06A-2, Y1-09A-1, Y1-09A-2, Y1-14A-1, Y1-14A-2); (e,f) cokeite (Y1-03C-1, Y1-03C-2, Y1-07C-1, Y1-07C-2, Y1-11C-1, Y1-11C-2, Y1-12C-1, Y1-12C-2, Y1-15C-1, Y1-15C-2); (g,h) coal (Y1-16S-1, Y1-16S-2, Y1-17S-1, Y1-17S-2, Y1-18S-1, Y1-18S-2, Y1-19S-1, Y1-19S-2, Y1-20S-1, Y1-20S-2).

The features of the above results can be summarised as follows: (1) the intensity ratio of Eg to Ag of pyrites increased significantly from the intrusion, via metamorphic aureole and cokeite, into unaffected coal. In addition, the Tg modes showed a weak and broad shoulder in all of the diagrams. (2) Almost all of the Raman frequencies of Eg (343.0–344.2) and Ag (377.4–380.6) shifted towards high frequencies relative to the shifts of Eg (343) and Ag (377) in the previously published Renishaw database. Additionally, there was an increasing trend of the FWHM values of Eg and Ag with increasing distance from the intrusion.

Table 1. Raman spectral data of pyrites.

Number	Sample	Position	(Eg)			(Ag)			(Tg)		
			$\Delta\nu_1/\text{cm}^{-1}$	I/103	F/cm ⁻¹	$\Delta\nu_1/\text{cm}^{-1}$	I/103	F/cm ⁻¹	$\Delta\nu_1/\text{cm}^{-1}$	I/103	F/cm ⁻¹
1	Y1-01R-1	intrusion	343.4	264.1	4.9	379.8	678.9	6.5	431.0	68.0	-
2	Y1-01R-2	intrusion	343.2	429.2	4.5	379.1	949.1	5.6	430.0	755.0	-
3	Y1-05R-1	intrusion	343.5	569.9	3.9	379.9	1126.9	4.7	431.0	91.0	-
4	Y1-05R-2	intrusion	343.6	558.1	3.9	380.0	1231.9	4.6	431.0	93.0	-
5	Y1-08R-1	intrusion	344.1	388.9	4.2	380.6	920.0	5.9	432.0	80.0	-
6	Y1-08R-2	intrusion	343.3	290.3	5.1	378.5	700.7	8.6	430.0	63.0	-
7	Y1-10R-1	intrusion	343.2	754.4	4.9	378.6	1463.2	6.5	429.0	72.0	-
8	Y1-10R-2	intrusion	343.9	735.1	3.7	380.5	1317.9	5.0	431.0	100.0	-
9	Y1-13R-1	intrusion	342.2	348.3	5.6	378.6	872.4	7.1	430.0	109.0	-
10	Y1-13R-2	intrusion	343.6	611.2	4.0	378.9	1258.6	5.5	433.0	119.0	-
11	Y1-02A-1	aureole	343.7	973.0	4.2	378.2	1349.0	5.6	-	-	-
12	Y1-02A-2	aureole	343.5	1074.2	5.0	377.9	1526.4	6.3	-	-	-
13	Y1-04A-1	aureole	343.2	680.7	7.1	377.6	864.4	7.7	-	-	-
14	Y1-04A-2	aureole	343.1	478.0	4.4	378.9	570.1	7.5	-	-	-
15	Y1-06A-1	aureole	343.1	560.0	6.8	379.0	609.1	6.0	-	-	-
16	Y1-06A-2	aureole	343.5	771.6	5.2	379.2	1122.7	7.1	-	-	-
17	Y1-09A-1	aureole	343.6	867.4	5.5	379.7	1215.3	6.7	-	-	-
18	Y1-09A-2	aureole	344.2	628.0	8.5	380.9	742.5	12.7	-	-	-
19	Y1-14A-1	aureole	344.5	647.3	8.1	380.4	889.5	12.8	-	-	-
20	Y1-14A-2	aureole	343.9	700.9	7.1	380.0	911.2	8.6	-	-	-
21	Y1-03C-1	cokeite	343.0	699.0	4.9	377.4	531.0	10.7	-	-	-

Table 1. Cont.

Number	Sample	Position	(Eg)			(Ag)			(Tg)		
			$\Delta\nu_1/\text{cm}^{-1}$	I/103	F/cm ⁻¹	$\Delta\nu_1/\text{cm}^{-1}$	I/103	F/cm ⁻¹	$\Delta\nu_1/\text{cm}^{-1}$	I/103	F/cm ⁻¹
22	Y1-03C-2	cokeite	343.5	896.8	5.7	379.7	874.1	8.8	-	-	-
23	Y1-07C-1	cokeite	343.4	892.3	5.7	379.4	869.7	8.6	-	-	-
24	Y1-07C-2	cokeite	343.1	930.1	5.9	378.9	923.9	7.4	-	-	-
25	Y1-11C-1	cokeite	343.7	904.8	8.1	379.2	832.9	9.9	-	-	-
26	Y1-11C-2	cokeite	343.6	994.1	5.9	377.1	1092.9	6.7	-	-	-
27	Y1-12C-1	cokeite	343.3	966.3	6.5	379.9	1020.0	7.9	-	-	-
28	Y1-12C-2	cokeite	342.0	1273.5	5.7	377.9	1099.5	7.0	-	-	-
29	Y1-15C-1	cokeite	344.8	804.0	8.5	380.9	775.8	13.4	-	-	-
30	Y1-15C-2	cokeite	344.0	913.2	7.7	379.4	928.7	10.3	-	-	-
31	Y1-16S-1	coal	322.7	925.1	10.2	386.1	121.2	11.2	-	-	-
32	Y1-16S-2	coal	323.2	516.3	6.7	391.9	84.6	8.6	-	-	-
33	Y1-17S-1	coal	324.1	781.7	7.3	387.2	259.4	7.3	-	-	-
34	Y1-17S-2	coal	326.3	1411.5	8.8	389.2	425.1	15.1	-	-	-
35	Y1-18S-1	coal	324.9	1510.6	5.3	387.9	100.7	4.0	-	-	-
36	Y1-18S-2	coal	325.9	1360.8	10.9	388.2	359.3	8.0	-	-	-
37	Y1-19S-1	coal	324.1	1249.5	9.3	387.1	512.9	8.9	-	-	-
38	Y1-19S-2	coal	326.2	717.7	10.9	394.3	232.3	20.9	-	-	-
39	Y1-20S-1	coal	324.8	1321.8	7.8	387.6	525.5	6.9	-	-	-
40	Y1-20S-2	coal	322.3	1897.1	4.6	386.4	256.8	4.1	-	-	-

3.3. LA-ICP-MS

The analytical results are shown in Table 2. The elements analysed include the total contents of iron and sulfur (FeS₂) and siderophile (V, Cr, Co, Ni) and sulphophile elements (As, Se, Bi, Sb) and other metals (Pb, Zn, Ag, Cu, REE). Most of these elements (Co, Ni, As, Se, Pb, Cu, Ag) had higher enrichment in the pyrites from the diabasic intrusion and metamorphic aureole than in those from the cokeite and coal. However, exceptions were encountered in some siderophile elements, for instance, the V content was very low (<4.2 ppm) in all of the pyrite types, but the Cr content was much lower in the pyrites from cokeite (0.32–1.2 ppm, average 0.64 ppm) than in the pyrites from the other occurrences (0.47–60 ppm, average 7.7 ppm). Both Co and Ni were not only strongly enriched in the pyrites from metamorphic aureole (Co = 148–1498 ppm and Ni = 93–1093 ppm) but were also strongly enriched in the pyrites from diabasic intrusion (Co = 2.3–416 ppm and Ni = 7.3–1051 ppm). The Co/Ni ratio of the pyrites from metamorphic aureole (1.0–2.9) was significantly higher than those of the pyrites from other occurrences (0.01–0.83). In addition, the contents of As (1.2–43 ppm) and Se (14–698 ppm) in the pyrites from metamorphic aureole were many times higher than those in the pyrites from other occurrences. Similarly, the Bi (0.03–28 ppm) and Sb (0.73–22 ppm) contents were higher in the pyrites from metamorphic aureole than from other occurrences. Many metallic elements were more enriched in the pyrites from diabasic intrusion and metamorphic aureole (especially the latter), for example, the Pb and Cu contents were 72–989 ppm and 9.2–478 ppm, respectively. In addition, REEs were strongly enriched (LREE = 0–258 ppm, HREE = 0–484 ppm) in the pyrites from unaffected coal.

Table 2. LA-ICP-MS geochemical results (ppm) of the pyrites from the Yuandian Coal Mine.

No.	Sample	Occurrence	FeS ₂	V	Cr	Co	Ni	As	Se	Bi	Sb	Pb	Zn	Cu	Ag	LREE	HREE
1	Y1-01R-1	intrusion	99.90	0.11	0.54	2.3	7.3	3.9	11	<0.01	0.08	12	0.47	3.6	0.06	<0.01	0.02
2	Y1-01R-2	intrusion	99.59	0.22	2.9	17	88	5.0	15	<0.01	1.2	50	0.66	43	1.3	0.90	0.47
3	Y1-05R-1	intrusion	99.51	0.06	1.4	32	64	21	29	<0.01	0.56	35	0.82	15	0.09	7.8	2.9
4	Y1-05R-2	intrusion	98.43	0.46	32	416	1051	12	21	0.05	0.80	176	1.0	33	0.76	0.93	0.33
5	Y1-8R-1	intrusion	99.66	0.04	4.3	39	164	12	33	0.01	0.56	72	0.35	29	0.24	0.79	0.20
6	Y1-8R-2	intrusion	99.47	0.16	13	28	113	12	50	0.01	0.69	165	0.71	14	0.48	0.65	0.25
7	Y1-10R-1	intrusion	97.09	0.53	56	132	401	26	32	0.02	2.4	383	1.5	55	0.63	0.74	0.22
8	Y1-10R-2	intrusion	98.88	0.16	20	31	205	10	18	0.01	1.5	51	0.95	16	0.27	1.4	0.55
9	Y1-13R-1	intrusion	98.60	0.30	32	67	368	22	28	0.01	1.7	159	1.2	39	0.29	1.5	0.38
10	Y1-13R-2	intrusion	99.79	0.05	3.7	11	114	9.6	39	<0.01	0.37	75	1.7	7.8	0.15	0.76	0.23
11	Y1-02-1	aureole	99.64	0.02	0.47	613	591	4.3	457	2.0	14	236	1.4	100	5.3	0.01	0.01
12	Y1-02-2	aureole	99.31	0.06	0.73	1498	1093	43	581	3.5	7.0	72	1.2	127	0.45	0.01	0.02
13	Y1-04-1	aureole	99.76	0.01	0.63	477	186	1.2	374	0.08	1.2	168	2.6	41	2.9	<0.01	0.02
14	Y1-04-2	aureole	98.47	4.3	60	148	93	3.1	14	0.03	3.2	407	1.2	19	1.8	0.49	0.30
15	Y1-06-1	aureole	99.34	0.01	0.40	761	262	10	681	0.44	2.6	111	1.2	70	1.5	0.01	0.01
16	Y1-06-2	aureole	87.85	4.4	68	1155	397	1.4	392	1.6	0.73	989	3.0	616	50	62	43
17	Y1-09-1	aureole	98.65	0.35	0.99	587	402	17	713	3.5	1.6	245	2.0	92	4.2	8.4	4.8
18	Y1-09-2	aureole	96.43	0.31	1.5	338	206	38	507	1.6	2.2	119	2.1	9.2	0.92	41	5.9
19	Y1-14-1	aureole	94.55	2.3	2.4	1467	719	30	501	28	22	521	5.8	478	24	7.4	5.1
20	Y1-14-2	aureole	98.94	0.14	1.1	546	232	6.2	698	3.8	2.9	219	2.1	113	6.2	1.1	1.1
21	Y1-03C-1	cokeite	99.95	0.05	0.85	2.4	26	<0.01	<0.01	<0.01	0.11	0.62	7.9	0.09	0.02	0.01	0.01
22	Y1-03C-2	cokeite	99.98	0.10	0.19	6.3	41	<0.01	0.50	<0.01	<0.01	1.1	0.37	<0.01	<0.01	0.02	0.04
23	Y1-07C-1	cokeite	99.97	0.04	0.70	1.1	2.2	0.11	<0.01	<0.01	0.03	6.2	0.80	0.29	<0.01	<0.01	0.01
24	Y1-07C-2	cokeite	99.98	0.03	0.32	0.08	<0.01	<0.01	0.53	<0.01	<0.01	0.02	0.35	0.02	0.01	0.01	0.02
25	Y1-11C-1	cokeite	99.98	0.12	0.58	0.09	0.17	0.46	6.6	<0.01	0.02	3.7	1.4	0.09	<0.01	0.01	0.01
26	Y1-11C-2	cokeite	99.98	0.03	0.44	0.32	0.39	0.04	1.8	<0.01	<0.01	0.45	0.51	0.03	<0.01	0.01	0.01
27	Y1-12C-1	cokeite	99.98	0.12	0.68	0.87	1.6	0.05	<0.01	<0.01	<0.01	0.41	0.86	0.29	<0.01	0.01	0.02
28	Y1-12C-2	cokeite	99.98	0.05	0.62	1.9	4.7	0.02	2.6	<0.01	<0.01	0.47	0.45	0.48	<0.01	<0.01	0.02
29	Y1-15C-1	cokeite	99.95	0.06	0.80	9.7	28	0.12	5.1	0.01	0.02	30	0.47	1.6	<0.01	0.01	0.01
30	Y1-15C-2	cokeite	99.94	0.09	1.2	1.3	12	0.03	<0.01	<0.01	0.08	0.54	8.2	0.75	<0.01	<0.01	0.03
31	Y1-16-1	coal	99.97	0.02	3.4	<0.01	0.07	<0.01	1.6	<0.01	<0.01	<0.01	2.8	<0.01	<0.01	0.01	0.01
32	Y1-17-1	coal	99.97	0.01	4.0	0.01	0.06	0.03	<0.01	<0.01	<0.01	<0.01	2.2	<0.01	0.01	0.01	0.01
33	Y1-18-1	coal	99.98	0.01	2.4	<0.01	0.05	0.02	<0.01	<0.01	<0.01	<0.01	1.7	0.05	<0.01	<0.01	<0.01
34	Y1-19-1	coal	99.97	0.02	2.6	<0.01	<0.01	0.12	2.8	<0.01	0.01	<0.01	3.1	0.01	<0.01	<0.01	0.03
35	Y1-20-1	coal	82.46	7.1	45	17	120	3.3	1.0	0.01	0.01	8.7	4.1	0.84	0.04	165	377
36	Y1-20-2	coal	82.70	6.2	32	16	50	27	1.1	0.05	0.23	11	68	2.9	0.05	258	484

4. Discussion

4.1. Relative Age of the Different Pyrite Generations

Pyrites in the diabase appeared as coarse-grain euhedral-subhedral crystals and fine veinlets, with the former commonly embedded in plagioclase and the latter extended around plagioclase. This indicates that the former is likely co-magmatic and the latter, late/post-magmatic [46–51]. In the metamorphic aureole, fine-grained pyrites were distributed mainly in the groundmass of the diabasic chilled margin, and only a few pyrite veinlets were found in/around the rims of mesocarbon microbeads in the cokeite. This indicates that the fine-grained pyrites were formed coevally with the groundmass [48–53], whilst pyrite veinlets were formed after the mesocarbon microbeads, which were post-magmatic as they crosscut the chilled margin [47–51]. Pyrites in the cokeite consisted mainly of veinlets and spherical aggregates, with the latter filling in the pores of cokeite and encapsulating large amounts of MCMB. This suggests that the pyrites in the cokeite were also likely formed after the mesocarbon [48–54]. Pyrites in the unaffected coal were dominated by framboidal aggregates, indicating that the pyrites were likely early diagenetic stages [51–53]. In summary, the pyrites from the Yuandian Coal Mine can be divided into four generations (Table 3), namely, the framboidal pyrites (Py I) in unaffected coal, coarse-grained pyrites (Py II) in diabase, pyrite veinlets (Py III) and fine-grained pyrites (Py III) in the metamorphic aureole, together with the pyrite veinlets (Py IV) and spherical pyrite aggregates (Py IV) in the intrusion-related cokeite.

Table 3. Occurrences of the different pyrite generations from the Yuandian coal mine.

Position	Intrusion Area	Aureole Area	Cokeite Area	Ordinary Coal Area	
Lithology	Diabase	Microporphyry	Coking Bitumen	Mesophase Carbon	Coal
Py I					Framboidal aggregate
Py II	Coarse-grained crystal				
Py III	Veinlet	Fine-grained crystal			
Py IV			Veinlet	Spherical aggregate	

4.2. Genesis of the Different Pyrite Generations

In the Raman spectra analysis, the Eg (322.3–326.2 cm^{-1}) and Ag (386.4–396.3 cm^{-1}) of pyrites in unaffected coal matched the reported frequency modes of marcasite [54–56], and the Eg (343.0–344.2) and Ag (377.4–380.6) of samples from diabase, aureole and cokeite shifted toward higher frequencies relative to the Eg (343) and Ag (377) of pyrite in the published Renishaw database [54–58]. This indicates that Py I may have deposited under relatively low temperatures [57–59]. The intensity ratios of Eg to Ag in pyrites increased away from the intrusion—the Eg values increased from 264.1–754.4 in Py II to 699.0–1273.5 in Py IV, whereas the Ag values decreased from 678.9–1243.2 in Py II to 531.0–1099.5 in Py IV. This indicates that the formation temperatures and pressures of Py II were higher than those of Py IV [56–59], as the intensity of Eg is negatively correlated with pressure, whereas the intensity of Ag is positively correlated with temperature [56–59]. Therefore, the pyrites enclosed in pyroxene and plagioclase (in diabase) have likely high formation temperatures [53–55], whilst the pyrites in the cokeite have likely low formation temperatures [53–58].

Our results show that the pyrite grains from the intrusions, aureole and cokeite differ in trace element contents (those of the pyrite from unaffected coal were mostly below the detection limits). It is

suggested that high Co/Ni ratios (>1) and high Se contents (>50 ppm) may reflect the hydrothermal genesis of pyrite [60–63]. In our work, the Co/Ni ratio in Py III was >1 (Figure 5a) and the Se contents were 72.37–989.27 ppm (Figure 5b), indicating that Py III may have been crystallized from magmatic-hydrothermal fluids [60–63].

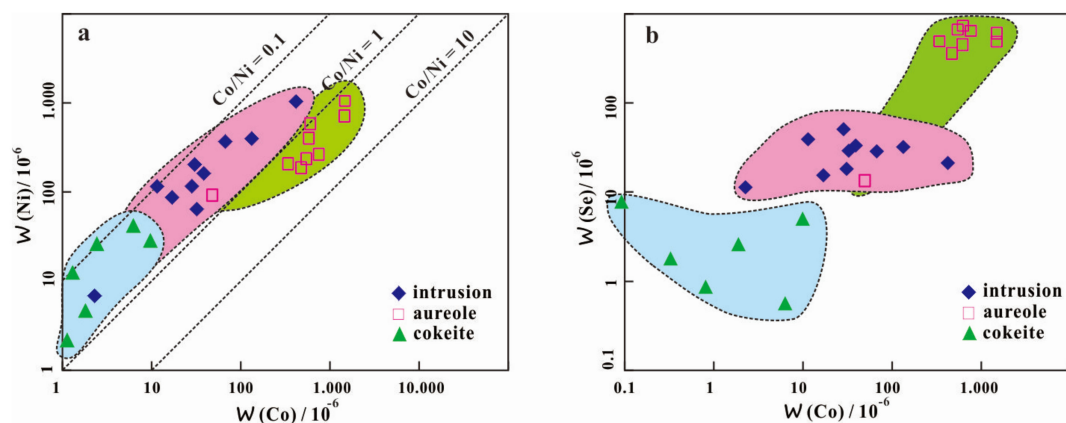


Figure 5. Binary diagrams of Ni, Se versus Co contents for different pyrite from the Yuandian Coal Mine. (a) Ni versus Co contents for different pyrite; (b) Se versus Co contents for different pyrite.

All evidence from the Raman spectra and trace elements above indicates that the pyrites in the diabase were likely of magmatic origin, whilst those in the metamorphic aureole may have been magmatic-hydrothermal fluid-derived, whilst the pyrites in the cokeite were likely of metasomatic origin. In brief, the genesis of pyrites at Yuandian included syngenetic-type (some metamorphosed along with the coalification) in the unaffected coal, magmatic-type (high temperature and pressure) in the diabasic intrusion, hydrothermal-type in metamorphic aureole and metasomatic-type with low temperature and low pressure in cokeite.

4.3. Geochemical Evolution of Pyrite

Pyrite compositions reflect the physicochemical conditions of the magmatic/hydrothermal/sedimentary system in which the pyrites are formed [63–65], thus the morphological and chemical changes of the four Yuandian pyrite generations can shed light on the migration and enrichment of different elements across the diabasic intrusions and the coal seams. Our results show that most siderophile and sulphophile elements analyzed are markedly enriched in the pyrites from the intrusion and metamorphic aureole. Concentrations of Co, Ni, As, Se, Pb and Cu of the pyrite crystals and veinlets from the metamorphic aureole were much higher than those in the intrusion, but they were both higher than their counterparts in the cokeite and unaffected coal. This suggests that the pyrites in the metamorphic aureole were likely crystallized from a fluid rich in these elements [63–65]. These elements (Co, Ni, As, Se, Pb and Cu) are likely magmatic-derived [64–67], as they were also enriched in the magmatic Py II (Figure 6). Meanwhile, these elements were relatively depleted in the pyrites from cokeite, suggesting that either these elements were scavenged by Py III before the fluids reached the cokeite to precipitate Py IV or that Py IV was precipitated from a fluid derived largely from the unaffected coal [63,64]. The geochemical data points to the toxic elements in the coal seams around the intrusions at Yuandian, notably Co, Ni, As, Se, Pb and Cu, mainly originating from regional mafic magmatism [66–69].

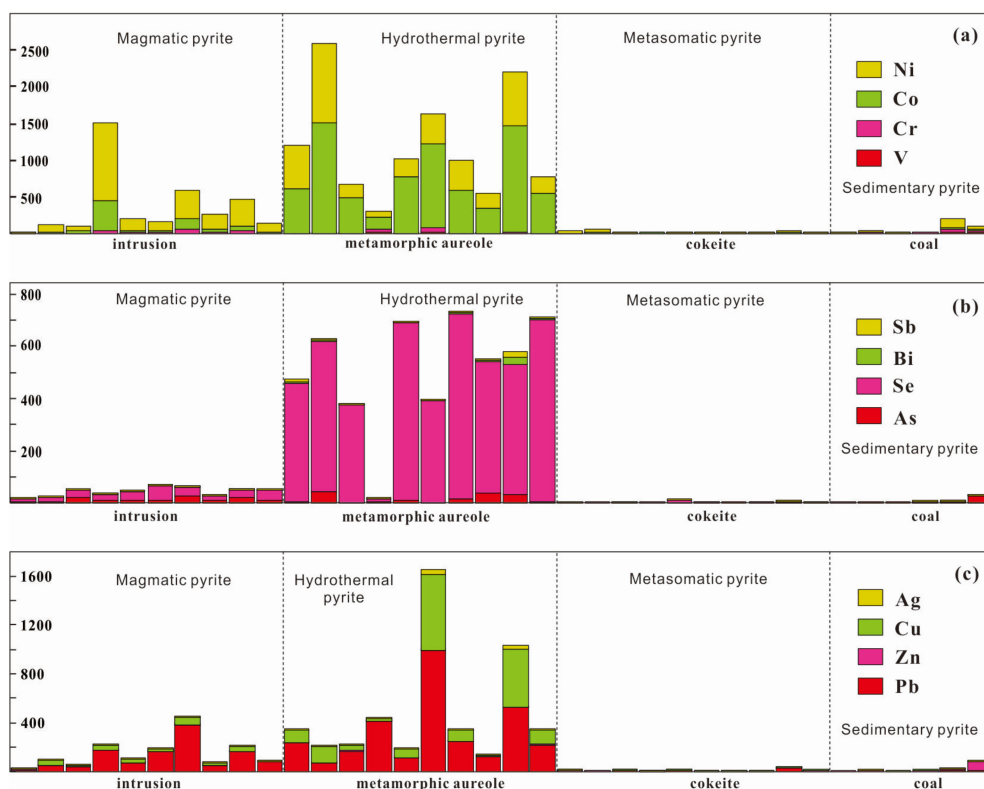


Figure 6. Histograms of element abundance in the different pyrite generations from the Yuandian Coal Mine. (a) Siderophile elements; (b) sulphophile elements; (c) metallic elements.

5. Conclusions

In this study, four pyrite generations in the Yuandian Coal Mine were identified, namely the framboidal syngenetic pyrite crystals in the unaffected coal, coarse-grained magmatic pyrites in the diabasic intrusions, fine-grained pyrites in the metamorphic aureole, and spheroid void-filling pyrite aggregates in the cokeite. The geochemical analyses of pyrite crystals in the studied coals indicate that the concentrations of toxic elements (notably Co, Ni, As, Se, Pb and Cu) in the pyrites from the metamorphic aureole were much higher than those from other occurrences. This suggests that the toxic elements in the Yuandian coal seam are derived by hydrothermal fluids that originate from the intrusions within the basin.

Acknowledgments: This work was supported by the National Natural Science Foundation of China (No. 41602173), Anhui University PhD Start-up Foundation (J10113190091) and the China Postdoctoral Science Foundation (2017M622020). Insightful comments from the editor and reviewers are deeply appreciated.

Author Contributions: Yanfei An was the chief investigator of the project and constructed the manuscript; Lingling Liu conducted the Raman spectroscopic analysis; Mina Wang conducted the optical microscopic observation, LA-ICP-MS analysis and data interpretation; Shuo Zheng performed the sampling, figure/diagram production and discussion; Yuanjie Guo conducted sampling, sample preparation and microscopic identification; Shuai Zhang conducted the field study and map production; Chunkit Lai conducted geochemical interpretation and manuscript editing.

Conflicts of Interest: The authors declare no conflict of interest.

References

1. Padwyssocki, M.H.; Dutcher, R.R. Coal dikes that intrude lamprophyre sills; Purgatoire River Valley, Colorado. *Econ. Geol.* **1971**, *66*, 267–280. [[CrossRef](#)]
2. Karayığit, A.I.; Whateley, M.K.G. Properties of a lacustrine subbituminous (K_1) seam, with special reference to the contact metamorphism, Soma-Turkey. *Int. J. Coal Geol.* **1977**, *34*, 131–155. [[CrossRef](#)]

3. Karayığit, A.I. Thermal Effects of a Basaltic Intrusion on the Soma Lignite Bed in West Turkey. *Energy Sources* **1998**, *20*, 55–66. [[CrossRef](#)]
4. Cooper, J.R.; Crelling, J.C.; Rimmer, S.M.; Whittington, A.G. Coal metamorphism by igneous intrusion in the Raton Basin, CO and NM: Implications for generation of volatiles. *Int. J. Coal Geol.* **2007**, *71*, 15–27. [[CrossRef](#)]
5. Walker, R.; Mastalerz, M.; Brassell, S.; Elswick, E.; Hower, J.C. Chemistry of thermally altered high volatile bituminous coals from southern Indiana. *Int. J. Coal Geol.* **2007**, *71*, 2–14. [[CrossRef](#)]
6. Mastalerz, M.; Drobniak, A.; Schimmelmann, A. Changes in optical properties, chemistry, and micropore characteristic of bituminous coal at the contact with dikes in the Illinois Basin. *Int. J. Coal Geol.* **2009**, *77*, 310–319. [[CrossRef](#)]
7. Sarana, S.; Kar, R. Effect of igneous intrusive on coal microconstituents: Study from an Indian Gondwana coalfield. *Int. J. Coal Geol.* **2011**, *85*, 161–167. [[CrossRef](#)]
8. Li, W.; Zhu, Y.; Chen, S.; Wang, H. The effects of igneous intrusions on coal-bed macerals, maturity, and adsorption. *Energy Sources Part A* **2017**, *39*, 58–66. [[CrossRef](#)]
9. Yao, Y.; Liu, D. Effects of igneous intrusions on coal petrology, pore-fracture and coalbed methane characteristics in Hongyang, Handan and Huaibei coalfields, North China. *Int. J. Coal Geol.* **2012**, *96*–97, 72–81. [[CrossRef](#)]
10. Matuszewska, A.; Pusz, S.; Duber, S. Evaluation of the structure of bituminous coal from Sośnica mine in the Upper Silesian Coal Basin (Poland) using reflectance indicating surface (RIS) parameters. *Int. J. Coal Geol.* **2015**, *152*, 177–188. [[CrossRef](#)]
11. Quaderer, A.; Mastalerz, M.; Schimmelmann, A.; Drobniak, A.; Bish, D.L.; Wintsch, R.P. Dike-induced thermal alteration of the Springfield Coal Member (Pennsylvanian) and adjacent clastic rocks, Illinois Basin, USA. *Int. J. Coal Geol.* **2016**, *166*, 108–117. [[CrossRef](#)]
12. Yoksoulia, L.E.; Rimmer, S.M.; Rowe, H.D. Anatomy of an intruded coal, II: Effect of contact metamorphism on organic $\delta^{13}\text{C}$ and implications for the release of thermogenic methane, Springfield (No. 5) Coal, Illinois Basin. *Int. J. Coal Geol.* **2016**, *158*, 129–136. [[CrossRef](#)]
13. Chen, S.; Wu, D.; Liu, G.; Sun, R. Raman spectral characteristics of magmatic-contact metamorphic coals from Huainan Coalfield, China. *Spectrochim. Acta A* **2017**, *171*, 31–39. [[CrossRef](#)] [[PubMed](#)]
14. An, Y.; Wang, M.; Liu, L.; Li, Y.; Cheng, J.; Liu, L. Microfabrics response of coal to magma among coal seam VIII in Yuandian Mine of Huaibei City, China. *J. China Coal Soc.* **2017**, *42*, 2975–2980, (In Chinese with English Abstract).
15. Rahman, M.W.; Rimmer, S.M.; Rowe, H.D. The impact of rapid heating by intrusion on the geochemistry and petrography of coals and organic-rich shales in the Illinois Basin. *Int. J. Coal Geol.* **2018**, *187*, 45–53. [[CrossRef](#)]
16. Shi, Q.; Qin, B.; Liang, H.; Gao, Y.; Bi, Q.; Qu, B. Effects of igneous intrusions on the structure and spontaneous combustion propensity of coal: A case study of bituminous coal in Daxing Mine, China. *Fuel* **2018**, *216*, 181–189. [[CrossRef](#)]
17. Singh, A.K.; Sharma, M.; Singh, M.P. Genesis of natural cokes: Some Indian examples. *Int. J. Coal Geol.* **2008**, *75*, 40–48. [[CrossRef](#)]
18. Rimmer, S.M.; Crelling, J.C.; Yoksoulia, L.E. An occurrence of coked bitumen, Raton Formation, Purgatoire River Valley, Colorado, USA. *Int. J. Coal Geol.* **2015**, *141*–142, 63–73. [[CrossRef](#)]
19. Mahesh, S.; Murthy, S.; Singh, V.P.; Roy, J.S. Thermally altered coals from bore core ebm-1, East Bokaro coal field, Damodar Valley, India: A petrographic inference. *J. Geol. Soc. India* **2015**, *86*, 535–546. [[CrossRef](#)]
20. Chen, H.; Jiang, J.; Chen, X.; Xu, C. Differences in coal bed methane occurrence for different regions of igneous erosion in the Haizi coal mine, Huaibei coalfield, China. *J. Nat. Gas Sci. Eng.* **2014**, *21*, 732–737. [[CrossRef](#)]
21. Guo, P.; Cheng, Y.; Jin, K.; Liu, Y. The impact of faults on the occurrence of coal bed methane in Renlou coal mine, Huaibei coalfield, China. *J. Nat. Gas Sci. Eng.* **2014**, *17*, 151–158.
22. Wang, L.; Liu, S.; Cheng, Y.; Yin, G.; Guo, P.; Mou, J. The effects of magma intrusion on localized stress distribution and its implications for coal mine outburst hazards. *Eng. Geol.* **2017**, *218*, 12–21. [[CrossRef](#)]
23. Karayığit, A.I.; Spears, D.A.; Booth, C.A. Antimony and arsenic anomalies in the coal seams from the Gokler coalfield, Gediz, Turkey. *Int. J. Coal Geol.* **2000**, *44*, 1–17. [[CrossRef](#)]

24. Diehl, S.F.; Goldhaber, M.B.; Hatch, J.R. Modes of occurrence of mercury and other trace elements in coals from the warrior field, Black Warrior Basin, Northwestern Alabama. *Int. J. Coal Geol.* **2004**, *59*, 193–208. [[CrossRef](#)]
25. Seredin, V.V.; Finkelman, R.B. Metalliferous coals: A review of the main geochemical types. *Int. J. Coal Geol.* **2008**, *76*, 253–289. [[CrossRef](#)]
26. Dai, S.; Zou, J.; Jiang, Y.; Ward, C.; Wang, X.; Li, T.; Xue, W.; Liu, S.; Tian, H.; Sun, X.; et al. Mineralogical and geochemical compositions of the Pennsylvanian coal in the Adaohai Mine, Daqingshan Coalfield, Inner Mongolia, China: Modes of occurrence and origin of diaspore, gorceixite, and ammonian illite. *Int. J. Coal Geol.* **2012**, *94*, 250–270. [[CrossRef](#)]
27. Diehl, S.F.; Goldhaber, M.B.; Koenig, A.E.; Lowers, H.A.; Ruppert, L.F. Distribution of arsenic, selenium, and other trace elements in high pyrite Appalachian coals: Evidence for multiple episodes of pyrite formation. *Int. J. Coal Geol.* **2012**, *94*, 238–249. [[CrossRef](#)]
28. Yang, M.; Liu, G.; Sun, R.; Chou, C.; Zheng, L. Characterization of intrusive rocks and REE geochemistry of coals from the Zhuji Coal Mine, Huainan Coalfield, Anhui, China. *Int. J. Coal Geol.* **2012**, *94*, 283–295. [[CrossRef](#)]
29. Chen, J.; Liu, G.; Li, H.; Wu, B. Mineralogical and geochemical responses of coal to igneous intrusion in the Pansan Coal Mine of the Huainan coalfield, Anhui, China. *Int. J. Coal Geol.* **2014**, *124*, 11–35. [[CrossRef](#)]
30. Dai, S.; Liu, J.; Ward, C.R.; Hower, J.C.; Xie, P. Petrological, geochemical, and mineralogical compositions of the low-Ge coals from the Shengli Coalfield, China: A comparative study with Ge-rich and a formation model for coal-hosted Ge ore deposit. *Ore Geol. Rev.* **2015**, *71*, 318–349. [[CrossRef](#)]
31. Dai, S.; Chekryzhov, I.Y.; Seredin, V.V.; Nechaev, V.P.; Graham, I.T.; Hower, J.C.; Ward, C.R.; Ren, D.; Wang, X. Metalliferous coal deposits in East Asia (Primorye of Russia and South China): A review of geodynamic controls and styles of mineralization. *Gondwana Res.* **2016**, *29*, 60–82. [[CrossRef](#)]
32. Karayığit, A.I.; Bircan, C.; Mastalerz, M.; Oskay, R.G.; Querol, X. Coal characteristics, elemental composition and modes of occurrence of some elements in the Isaalan coal (Balıkesir, NW Turkey). *Int. J. Coal Geol.* **2017**, *172*, 43–59. [[CrossRef](#)]
33. Karayığit, A.I.; Mastalerz, M.; Oskay, R.G.; Gayer, R.A. Coal petrography, mineralogy, elemental compositions and palaeoenvironmental interpretation of Late Carboniferous coal seams in three wells from the Kozlu coalfield (Zonguldak Basin, NW Turkey). *Int. J. Coal Geol.* **2017**, *187*, 54–70. [[CrossRef](#)]
34. Zheng, L.; Sun, R.; Hintelmann, H.; Zhu, J.; Wang, R.; Sonke, J.E. Mercury stable isotope compositions in magmatic-affected coal deposits: New insights to mercury sources, migration and enrichment. *Chem. Geol.* **2018**, *479*, 86–101. [[CrossRef](#)]
35. Zhao, L.; Ward, C.R.; French, D.; Graham, I.T.; Dai, S.; Yang, C.; Xie, P.; Zhang, S. Origin of a kaolinite-NH₄-illite-pyrophyllite-chlorite assemblage in a marine-influenced anthracite and associated strata from the Jincheng Coalfield, Qinshui Basin, Northern China. *Int. J. Coal Geol.* **2018**, *185*, 61–78. [[CrossRef](#)]
36. Dai, S.; Ren, D. Effects of magmatic intrusion on mineralogy and geochemistry of coals from the Fengfeng-Handan Coalfield, Hebei, China. *Energy Fuels* **2007**, *21*, 1663–1673. [[CrossRef](#)]
37. Wang, X.; Jiang, Y.; Zhou, G.; Wang, P.; Wang, R.; Zhao, L.; Chou, C. Behavior of minerals and trace elements during natural coking: A case study of an intruded bituminous coal in the Shuoli mine, Anhui Province, China. *Energy Fuels* **2015**, *29*, 4100–4113. [[CrossRef](#)]
38. An, Y.; Liu, B.; Zhu, Q.; Sun, Y.; Zhu, X. Mechanism of REE in metamorphic belt between coal and intrusion from Wolonghu mine of Anhui, China. *Chin. Rare Earths* **2017**, *38*, 47–55, (In Chinese with English Abstract).
39. An, Y.; Zheng, L.; Sun, Q.; Jiang, Y.; Wang, C.; Wang, R.; Niu, K. Micro-Raman spectral characteristics and implication of FeS₂ from metamorphic belt between coal and intrusion in Wolonghu mine of Anhui Province, China. *Spectrosc. Spectr. Anal.* **2016**, *36*, 986–990, (In Chinese with English Abstract).
40. Cheng, H.; Liu, Q.; Zhang, S.; Wang, S.; Frost, R.L. Evolved gas analysis of coal-derived pyrite/marcasite. *J. Therm. Anal. Calorim.* **2014**, *116*, 887–894. [[CrossRef](#)]
41. Kolker, A. Minor element distribution in iron disulfides in coal: A geochemical review. *Int. J. Coal Geol.* **2012**, *94*, 32–43. [[CrossRef](#)]
42. Susilawati, R.; Ward, C.R. Metamorphism of mineral matter in coal from the Bukit Asam deposit, south Sumatra, Indonesia. *Int. J. Coal Geol.* **2006**, *68*, 171–195. [[CrossRef](#)]

43. Zhao, H.; Bai, Z.; Yan, J.; Bai, J.; Li, W. Transformations of pyrite in different associations during pyrolysis of coal. *Fuel Process. Technol.* **2015**, *131*, 304–310. [[CrossRef](#)]
44. Dai, S.; Wang, X.; Seredin, V.V.; Hower, J.C.; Ward, C.R.; O'Keefe, J.M.K.; Huang, W.; Li, T.; Li, X.; Liu, H.; et al. Petrology, mineralogy, and geochemistry of the Ge-rich coal from the Wulantuga Ge ore deposit, Inner Mongolia, China: New data and genetic implications. *Int. J. Coal Geol.* **2012**, *90–91*, 72–99. [[CrossRef](#)]
45. Duan, P.; Wang, W.; Liu, X.; Qian, F.; Sang, S.; Xu, S. Distribution of As, Hg and other trace elements in different size and density fractions of the Reshuihe high-sulfur coal, Yunnan Province, China. *Int. J. Coal Geol.* **2017**, *173*, 129–141. [[CrossRef](#)]
46. Dai, S.; Ren, D.; Tang, Y.; Shao, L.; Li, S. Distribution, isotopic variation and origin of sulfur in coals in the Wuda coalfield, Inner Mongolia, China. *Int. J. Coal Geol.* **2002**, *51*, 237–250. [[CrossRef](#)]
47. Dai, S.; Hou, X.; Ren, D.; Tang, Y. Surface analysis of pyrite in the No. 9 coal seam, Wuda Coalfield, Inner Mongolia, China, using high-resolution time-of-flight secondary ion mass-spectrometry. *Int. J. Coal Geol.* **2003**, *55*, 139–150. [[CrossRef](#)]
48. Chou, C. Sulfur in coals: A review of geochemistry and origins. *Int. J. Coal Geol.* **2012**, *100*, 1–13. [[CrossRef](#)]
49. Querol, X.; Chinchon, S.; Lopez-Soler, A. Iron sulfide precipitation sequence in Albian coals from the Maestrazgo Basin, southeastern Iberian Range, northeastern Spain. *Int. J. Coal Geol.* **1989**, *11*, 171–189. [[CrossRef](#)]
50. Kortenski, J.; Kostova, I. Occurrence and morphology of pyrite in Bulgarian coals. *Int. J. Coal Geol.* **1996**, *29*, 273–290. [[CrossRef](#)]
51. Xue, J.; Li, S.; Sun, W.; Zhang, Y.; Zhang, X. Characteristics of the genetic mineralogy of pyrite and its significance for prospecting in the Denggezhuang gold deposit, Jiaodong Peninsula, China. *Sci. China Earth Sci.* **2014**, *57*, 644–661. [[CrossRef](#)]
52. Xie, Q.; Chen, T.; Fan, Z.; Xu, X.; Zhou, Y.; Shi, W.; Xie, J. Morphological characteristics and genesis of colloform pyrite in Xinqiao Fe-S deposit, Tongling, Anhui Province. *Sci. Sin. Terrae* **2017**, *44*, 2665–2674, (In Chinese with English Abstract).
53. An, Y.; Li, X.; Wang, Y.; Zhu, Q.; Liu, B.; Zhang, W.; Zheng, L.; Nenzhelele, J.D.N. The ultra structure significance of pyrite from the Pozaiying porphyry molybdenum deposits in southern section of Qinzhou-Hangzhou metallogenic belt. *Acta Petrol. Sin.* **2017**, *33*, 729–738, (In Chinese with English Abstract).
54. An, Y.; Jiang, D.; Zhong, L. Micro-Raman spectral characteristics and implication of FeS₂ from augen granites in west of Guangdong. *Spectrosc. Spectr. Anal.* **2014**, *34*, 2439–2443, (In Chinese with English Abstract).
55. Blanchard, M.; Alfredsson, M.; Brodholt, J.; Price, G.D.; Wright, K.; Catlow, C.R.A. Electronic structure study of the high-pressure vibrational spectrum of FeS₂ pyrite. *J. Phys. Chem. B* **2005**, *109*, 22067–22073. [[CrossRef](#)] [[PubMed](#)]
56. Schmokel, M.S.; Bjerg, L.; Cenedese, S.; Jorgensen, M.R.V.; Chen, Y.S.; Overgaard, J.; Iversen, B.B. Atomic properties and chemical bonding in the pyrite and marcasite polymorphs of FeS₂: A combined experimental and theoretical electron density study. *Chem. Sci.* **2014**, *5*, 1408–1421. [[CrossRef](#)]
57. Kleppe, A.K.; Jephcoat, A.P. High-pressure Raman spectroscopic studies of FeS₂ pyrite. *Mineral. Mag.* **2004**, *68*, 433–441. [[CrossRef](#)]
58. Utyuzh, A.N. Influence of temperature on Raman spectra of the FeS₂ single crystal with pyrite structure. *Phys. Solid State* **2014**, *56*, 2050–2055. [[CrossRef](#)]
59. Yuan, X.; Zheng, H. In situ Raman spectroscopic studies of FeS₂ pyrite up to 675 K and 2100 MPa using a hydrothermal diamond anvil cell. *Mineral. Mag.* **2015**, *79*, 1–10. [[CrossRef](#)]
60. Clark, C.; Grguric, B.; Schmidt, M.A. Genetic implications of pyrite chemistry from the Palaeoproterozoic Olary Domain and overlying Neoproterozoic Adelaidean sequences, northeastern South Australia. *Ore Geol. Rev.* **2004**, *25*, 237–257. [[CrossRef](#)]
61. Koglin, N.; Frimmel, H.E.; Minter, W.E.L.; Brätz, H. Trace-element characteristics of different pyrite types in Mesoarchean to Palaeoproterozoic placer deposits. *Miner. Depos.* **2010**, *45*, 259–280. [[CrossRef](#)]
62. Large, R.R.; Mukherjee, I.; Gregory, D.D. Ocean and Atmosphere Geochemical Proxies Derived from Trace Elements in Marine Pyrite: Implications for Ore Genesis in Sedimentary Basins. *Econ. Geol.* **2017**, *112*, 423–450. [[CrossRef](#)]
63. Zhao, Z. *Geochemical Principles of Trace Element*; Science Press: Beijing, China, 2016; ISBN 978-7-03-047496-4.

64. Xiao, X.; Zhou, T.; Fan, Y.; Xie, J.; Zhang, L. LA-ICP-MS in situ trace elements and FE-SEM analysis of pyrite from the Xinqiao Cu-Au-S deposit in Tongling, Anhui and its constraints on the ore genesis. *Acta Petrol. Sin.* **2016**, *32*, 369–376, (In Chinese with English Abstract).
65. Dehnavi, A.S.; McFarlane, C.R.M.; Lentz, D.R.; Walker, J.A. Assessment of pyrite composition by LA-ICP-MS techniques from massive sulfide deposits of the Bathurst Mining Camp, Canada: From textural and chemical evolution to its application as a vectoring tool for the exploration of VMS deposits. *Ore Geol. Rev.* **2018**, *92*, 656–671. [[CrossRef](#)]
66. Zhou, L.; McKenna, C.A.; Long, D.G.F.; Kamber, B.S. LA-ICP-MS elemental mapping of pyrite: An application to the Palaeoproterozoic atmosphere. *Precambrian Res.* **2017**, *297*, 33–55. [[CrossRef](#)]
67. Keith, M.; Häckel, F.; Haase, K.M.; Schwarz-Schampera, U.; Klemm, R. Trace element systematics of pyrite from submarine hydrothermal vents. *Ore Geol. Rev.* **2016**, *72*, 728–745. [[CrossRef](#)]
68. Deng, J.; Wen, S.; Chen, X.; Xian, Y.; Wu, D. Dynamic simulation of the thermal decomposition of pyrite under vacuum. *Metall. Mater. Trans. A* **2014**, *45*, 2445–2452. [[CrossRef](#)]
69. Sharma, R.; Srivastava, P.K. Hydrothermal fluids of magmatic origin. In *Modelling of Magmatic and Allied Processes*; Kumar, S., Singh, R.N., Eds.; Springer International Publishing: Cham, Switzerland; Berlin, Germany, 2014; pp. 181–209, ISBN 978-3-319-06470-3.



© 2018 by the authors. Licensee MDPI, Basel, Switzerland. This article is an open access article distributed under the terms and conditions of the Creative Commons Attribution (CC BY) license (<http://creativecommons.org/licenses/by/4.0/>).